

Cite this: *New J. Chem.*, 2012, **36**, 2405–2411

www.rsc.org/njc

PAPER

One pot synthesis of hard phase $\text{Nd}_2\text{Fe}_{14}\text{B}$ nanoparticles and $\text{Nd}_2\text{Fe}_{14}\text{B}/\alpha\text{-Fe}$ nanocomposite magnetic materials

Abhijit P. Jadhav,^a Abid Hussain,^a Jae Ho Lee,^a Youn Kyung Baek,^b
Chul Jin Choi^b and Young Soo Kang^{*a}

Received (in Montpellier, France) 25th May 2012, Accepted 3rd September 2012

DOI: 10.1039/c2nj40620a

Nanophase materials with an average grain size in the range of 1 to 50 nm have attracted research interest for more than a decade since their physical properties are quite different from that of their bulk micron-sized counterparts. The properties of magnetic materials are highly dependent on its particle size. The synthesis of hard phase magnetic nanoparticles was carried out in a one pot reaction. By controlling the reaction conditions, the exchange coupling between the hard and soft phase in the hard/soft nanocomposite magnetic material has been studied. The reaction parameters, such as the ratio of the metallic precursors, reaction temperature and reduction process, play an important role in determining the shape and size of the material along with its magnetic properties. To produce the exchange coupling between hard and soft phases their particle size needs to be controlled very precisely, which can help to increase the interaction between the two phases. By controlling the ratio of precursors, the amount of soft phase of $\alpha\text{-Fe}$ was optimized for the synthesis *in situ* with the hard phase $\text{Nd}_2\text{Fe}_{14}\text{B}$ material.

1. Introduction

One of the important permanent magnetic materials offering high coercivity and an energy product is $\text{Nd}_2\text{Fe}_{14}\text{B}$, which was discovered by Sagawa *et al.*¹ $\text{Nd}_2\text{Fe}_{14}\text{B}$ magnetic material is the highest energy product material available to date and many reviews are available in the literature.^{2–4} The higher anisotropy field value of this magnetic material has given rise to larger coercivity and hence its energy product is higher. The energy product is defined as the area enclosed in the second quadrant of the $B\text{--}H$ loop and hence high magnetization and coercivity values give rise to high energy products. The energy product of the single phase magnet initially reported was 320 kJ m^{-3} , and with considerable research it has now reached a maximum of over 440 kJ m^{-3} .⁵ Since the energy product is inversely proportional to the volume of the magnet, a higher energy product leads to miniaturized magnets. However, the single phase $\text{Nd}_2\text{Fe}_{14}\text{B}$ magnet has some drawbacks like a very low Curie temperature of 585 K and also they are highly corrosive in nature.

Exchange coupled nanocomposites are composed of a combination of hard and soft phase magnets for the achievement

of a higher energy product. The large energy product was obtained from the combination of high coercivity and a large remanence value as compared to the traditional single phase material. Various efforts have been made to prepare nanocomposite magnets with the combination of Fe/SmCO_5 ⁶ and $\text{Nd}_2\text{Fe}_{14}\text{B}/\alpha\text{-Fe}$ ⁷ by controlling the size and proportion of hard and soft magnetic particles. Such nanocomposite magnetic materials are called exchange spring magnets which are describe in detail by Kneller and Hawig.⁸

The conventional or industrial methods of production of the magnetic materials are based on processes such as induction melting, crushing, ball milling, *etc.*^{9,10} The major drawbacks of these conventional methods is the difficulty in maintaining the alloy composition, particle size control and the final shape of the magnetic materials.^{11,12} To overcome these problems, a large amount of research has been carried out in the area of magnetism and magnetic materials, which is a rich combination of chemical synthesis techniques, characterization, theoretical concepts and engineering applications.¹³ Rare earth based permanent magnets have a very broad range of technological applications due to their excellent combination of high coercivity and energy product $(BH)_{\text{max}}$. Hard magnetic materials have various applications as voice coil motors in hard disk drives, communication devices, MRI, traveling wave tubes and in a variety of house hold products, permanent magnets, data storage analogs, and digital data storage and quantum devices for which a large coercivity and remanence value is a basic requirement.¹⁴ To achieve these requirements for the preparation of the magnetic materials, the solution

^a Department of Chemistry, Sogang University, 1, Shinsu-dong, Mapo-gu, Seoul 121-742, Republic of Korea.
E-mail: yskang@sogang.ac.kr; Fax: +82 2 701 0967;
Tel: +82 2 705 8882

^b Korea Institute of Materials Science, 797 Changwondero, Seongsan-gu, Changwon, Gyeongnam 642 831, Republic of Korea.
Fax: +82 55 280 3289; Tel: +82 55 280 3532

phase chemical synthesis approaches have been applied to prepare monodispersed soft phase magnetic nanoparticles and have recently been extended to the synthesis of hard phase magnets such as SmCo_5 nanoparticles by coupling the polyol reduction of rare earth precursors.^{15–18} Other chemical synthesis methods includes sol–gel and novel autocombustion reduction diffusion synthesis, which have been reported by the Ramanujan group.^{7,19}

Synthesis of $\text{Nd}_2\text{Fe}_{14}\text{B}$ by chemical routes offers the possibility of size and shape control by optimizing the nucleation rate and growth of particles.²⁰ The nanoparticle size can be controlled by adjusting the parameters such as reaction time, temperature and concentration of reagents.²¹ The method of glycine nitrate autocombustion was developed by Chick *et al.* in 1990 for the synthesis of metal oxides.²² This method has several advantages over other chemical methods, such as mixing of metal ions and could be carried out very efficiently at a molecular level. It also helps to form homogeneously mixed powders. For the combustion of metallic precursors, various kinds of fuels such as glycine, urea, citric acid and glycerol have been used.^{23–25}

In this article we report the synthesis of $\text{Nd}_2\text{Fe}_{14}\text{B}$ hard phase magnetic material and $\text{Nd}_2\text{Fe}_{14}\text{B}/\alpha\text{-Fe}$, a hard/soft phase nanocomposite magnetic materials, by a glycine nitrate autocombustion reduction diffusion method.²⁰ The method includes the conversion of metal nitrate precursors to metal oxides *via* complex formation with glycine. The variation of metallic ratio helps to produce hard phase $\text{Nd}_2\text{Fe}_{14}\text{B}$ as well as a hard/soft mixture of $\text{Nd}_2\text{Fe}_{14}\text{B}/\alpha\text{-Fe}$ *via* the one pot reaction. Controlling of reaction parameters can be helpful for phase selectivity and the molar ratio of the synthesized magnetic phases of the nanostructured composite materials. A well dispersed and homogeneous size distribution of $\text{Nd}_2\text{Fe}_{14}\text{B}$ and $\text{Nd}_2\text{Fe}_{14}\text{B}/\alpha\text{-Fe}$ nanostructures can be synthesized by this method.

2. Experimental

2.1 Materials

Neodymium(III) nitrate hexahydrate [$\text{Nd}(\text{NO}_3)_3 \cdot 6\text{H}_2\text{O}$, 99.9%, Aldrich Chemicals], iron(II) nitrate nonahydrate [$\text{Fe}(\text{NO}_3)_3 \cdot 9\text{H}_2\text{O}$, $\geq 98\%$, Sigma Aldrich], boric acid (H_3BO_3 , 99.9%, Katayama Chemicals), glycine ($\text{C}_2\text{H}_5\text{O}_2\text{N}$, 98%, Aldrich Chemicals), were used as received without further purification and de-ionized (DI) water as a solvent.

2.2 Synthesis

2.2.1 Synthesis of metal oxide mixtures. The general synthesis scheme is represented in Fig. 1. The precursors of metal nitrates $\text{Nd}(\text{NO}_3)_3 \cdot 6\text{H}_2\text{O}$, $\text{Fe}(\text{NO}_3)_3 \cdot 9\text{H}_2\text{O}$ and boric acid were taken in two different molar ratios of Nd:Fe:B = 15:77.5:7.5 (for $\text{Nd}_2\text{Fe}_{14}\text{B}$ phase) and 2:9.5:1 (for $\text{Nd}_2\text{Fe}_{14}\text{B}/\alpha\text{-Fe}$ mixed phase). The precursors were dissolved in 25 mL DI water in a separate flasks with magnetic stirring at room temperature for around 10 min. A 25 mL of glycine solution was prepared by dissolving glycine in DI water in a molar ratio of metal: glycine as 1:1.

The glycine solution was added slowly to the metal nitrate solutions. The light orange color changed to dark red after the addition of two solutions. The water was evaporated by

heating the solution at 200 °C on a hot plate with continuous magnetic stirring. As the water starts to evaporate the solution viscosity increases. When all of water is evaporated, the remaining viscous mass ignites and burns spontaneously to give a mixture of the metal oxides. The as-prepared metal oxides were washed with DI water to remove any soluble impurities and later with ethanol to remove any carbon containing impurities. The sample was dried at 60 °C in air before it was reduced.

2.2.2 Reduction treatment. The metal oxides were reduced to NdFeB and $\text{NdFeB}/\alpha\text{-Fe}$ nanostructures in an Ar + 5% H_2 atmosphere at 950 °C for 2 h under vacuum. After the reduction treatment, the samples were cooled to room temperature and immediately transferred to an organic solvent, such as hexane, and was stored for further characterization. During the heat treatment at high temperature, the metals, such as neodymium, iron and boron, diffuse into each other to form $\text{Nd}_2\text{Fe}_{14}\text{B}$ alloy. It may also be possible that neodymium and boron diffuse out separately instead of forming an alloy. It is for this reason we obtained different molar ratios for the precursors and final product. The loss of neodymium and boron is only a small fraction of the total mass.

2.3 Characterizations

X-ray diffraction (XRD) patterns of the as-prepared metal oxides and reduced NdFeB , $\text{NdFeB}/\alpha\text{-Fe}$ composite magnetic materials were recorded using the Cu K α radiation ($\lambda = 1.54056 \text{ \AA}$) of a Rigaku Miniflex-II desktop X-ray diffractometer operating at 30 kV and 15 mA. The samples were scanned at the rate of 0.05° per second in the range of $2\theta = 10\text{--}80^\circ$. The size and shape of the as-synthesized nanostructures were examined with a JEOL JEM 2100 F transmission electron microscope (TEM) operating at 200 kV. For TEM observations, the samples were dispersed in hexane with 1–2 drops of ethanol in it. The drop of the well dispersed nanoparticles were placed over the carbon coated microscopic copper grids (200 mesh size) and were subsequently dried. Elemental mapping and energy dispersive X-ray spectroscopy analysis (EDX) were carried out on a JEOL JEM 2100 F scanning transmission electron microscope equipped with an energy dispersive X-ray spectroscopy analyser. The magnetic properties of the as-prepared magnetic nanostructures were measured at room temperature using a vibrating sample magnetometer (VSM) (LakeShore 7400) with an external magnetic field up to 14 000 Gauss.

3. Result and discussion

The success of the process is due to intimate blending among the metal salts using a suitable fuel or complexing agent (glycine in this case) in an aqueous medium and an exothermic redox reaction between the fuel and oxidizers (nitrates).²⁵ The various factors which are responsible for controlling the reaction are the fuel type, ratio of fuel (glycine) and metal nitrates, reaction temperature and the amount of water in the precursor mixture. A general mechanism for the formation of the metal oxides through the glycine autocombustion method is shown in Fig. 1. The metal nitrate salts, after dissociation in aqueous solution, form metal cations. The amino acid in

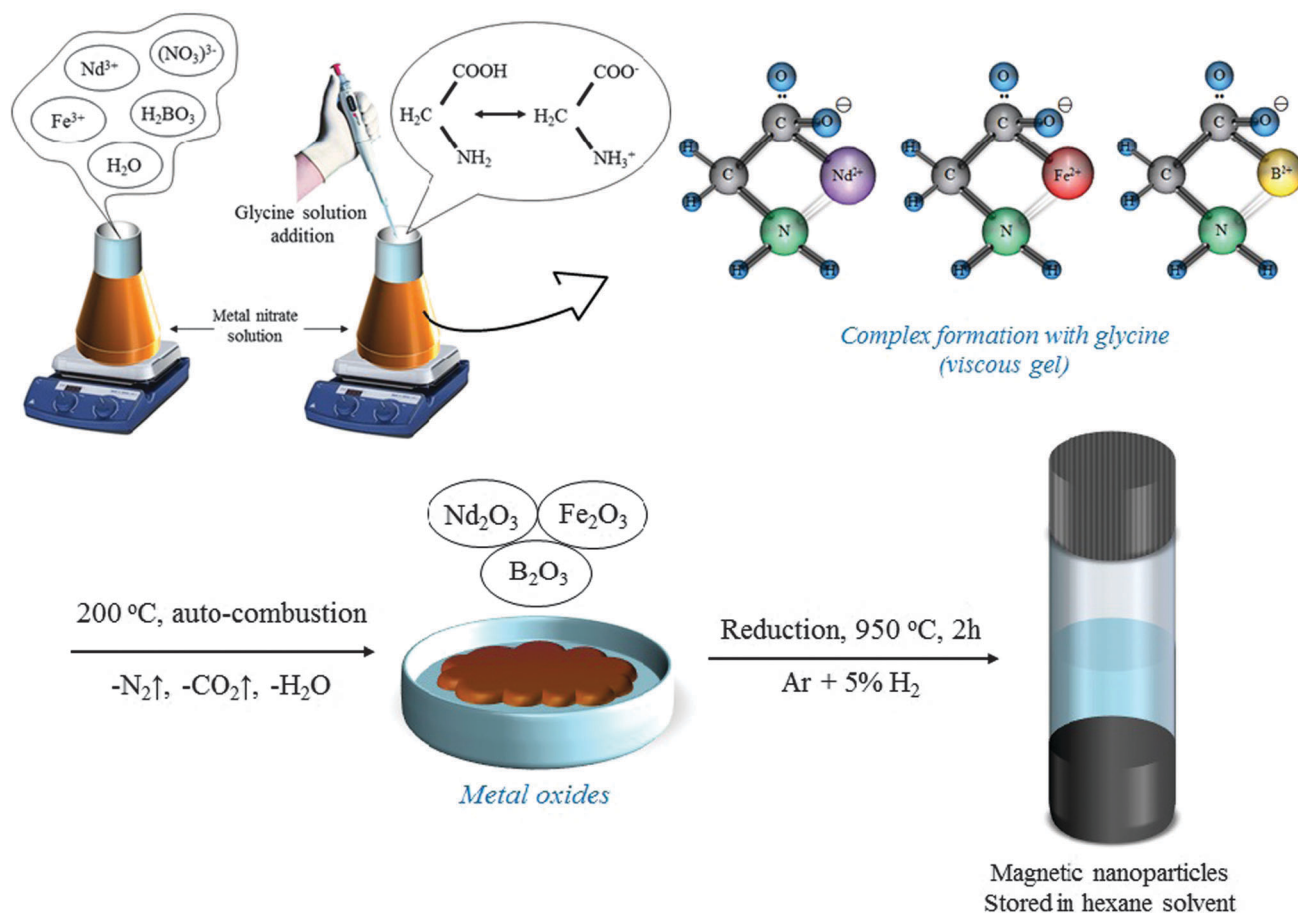


Fig. 1 Schematic representation of the general synthesis used for preparation of $\text{Nd}_2\text{Fe}_{14}\text{B}$ and $\text{Nd}_2\text{Fe}_{14}\text{B}/\alpha\text{-Fe}$ magnetic nanoparticles by the glycine autocombustion method.

glycine, after addition in aqueous solution, becomes a zwitter ion with both positive and negative charges, which forms a complex with the metal cations. The metal cations form a complex by attaching to the bidentate ligand of the glycine molecule. After addition of glycine, as the metal cations form a complex with the glycine molecule, it helps to prevent selective precipitation and it also helps to maintain a uniform metal composition ratio over all constituents. During the formation of the complex, the viscosity of the solution increases as the water is removed, due to the high temperature. Glycine also helps the solubility of the metal ions to avoid phase separation during evaporation of the water at $200\text{ }^\circ\text{C}$. Once all of the water is removed the viscous mass gets ignited (autocombustion process) and the viscous mass burns out to form a mixture of metal oxides with the evolution of N_2 , H_2O and CO_2 gases, which are environmentally non-hazardous. The autocombustion method helps to increase the crystallinity of the metal oxides.

Fig. 2 shows XRD pattern of the as-prepared $\text{Nd}_2\text{Fe}_{14}\text{B}$ nanoparticles after heat treatment at $950\text{ }^\circ\text{C}$ for 2 h in an $\text{Ar} + 5\% \text{H}_2$ gas atmosphere of the sample which was prepared from the molar ratio of $\text{Nd}:\text{Fe}:\text{B} = 15:77.5:7.5$ (for $\text{Nd}_2\text{Fe}_{14}\text{B}$). The XRD pattern shows a good match with the standard diffraction pattern of $\text{Nd}_2\text{Fe}_{14}\text{B}$ [JCPDS card no. – 39-0473, tetragonal, $P4_2/mnm$ (136)]. The sharpness of the peaks indicates good crystallinity in the sample. Most of the

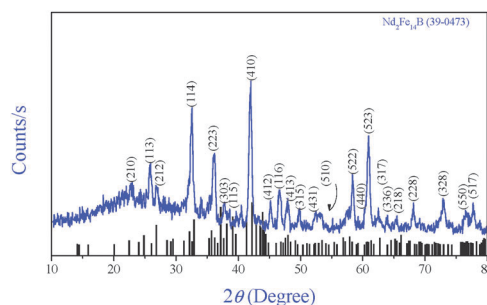


Fig. 2 XRD pattern of $\text{Nd}_2\text{Fe}_{14}\text{B}$ nanoparticles after reduction treatment at $950\text{ }^\circ\text{C}$ for 2 h in an $\text{Ar} + 5\% \text{H}_2$ gas atmosphere under vacuum.

peaks were matching well with the standard JCPDS cards with one or two exceptions, like the (214) plane, which might be due to some kind of impurity or crystal defect. The sample shows no other phase than $\text{Nd}_2\text{Fe}_{14}\text{B}$, and no peaks related to oxygen and other impurities were recorded. The peaks represent good crystallinity in the nanostructure after the reduction treatment at $950\text{ }^\circ\text{C}$ for 2 h in an $\text{Ar} + 5\% \text{H}_2$ atmosphere.

For the second case, the XRD pattern of $\text{Nd}_2\text{Fe}_{14}\text{B}/\alpha\text{-Fe}$ nanoparticle mixture prepared by the heat treatment at $950\text{ }^\circ\text{C}$ for 2 h in an $\text{Ar} + 5\% \text{H}_2$ gas atmosphere is shown in Fig. 3. The XRD pattern shows a good match with the peaks of the

standard JCPDS card of $\text{Nd}_2\text{Fe}_{14}\text{B}$ [39-0473, tetragonal, $P4_2/mnm$ (136)] and $\alpha\text{-Fe}$ [06-0696, cubic, $Im\bar{3}m$ (229)]. In this case, as a soft phase $\alpha\text{-Fe}$ is present in the dominant state of the main peak of (410) for $\text{Nd}_2\text{Fe}_{14}\text{B}$, and was dominated by the peak of $\alpha\text{-Fe}$ (110) at $2\theta = 44.65^\circ$.

The particle size and nature of crystallinity of $\text{Nd}_2\text{Fe}_{14}\text{B}$ and $\text{Nd}_2\text{Fe}_{14}\text{B}/\alpha\text{-Fe}$ were determined by transmission electron microscopy images and are represented in Fig. 4 and 5. The $\text{Nd}_2\text{Fe}_{14}\text{B}$ nanoparticles are almost spherical in shape with an average particle size of around 25 nm. We also found in some places, that nanoparticles had agglomerated to form large size structures. The extended growth of the nanoparticles was due to the high temperature heat treatment and the absence of any protecting medium to restrict their growth. The particle size of $\text{Nd}_2\text{Fe}_{14}\text{B}$ was also confirmed by calculation of the crystallite size by the Debye–Scherrer equation. The size calculated at various diffraction peaks such as, (114), (223), (410) and (227) was around 18.33, 15.26, 15.21 and 31.51 nm, respectively. The estimation of particle size from the Debye–Scherrer calculation shows that the nanoparticles are composed of the same $\text{Nd}_2\text{Fe}_{14}\text{B}$ phase. Thus it was confirmed that the nanoparticles with a size of around 24.73 ± 4.205 nm were present to a large extent, except in a few cases where we found large sized nanostructures. The large sized agglomerated particle was chosen over the small nanoparticles for the analysis of HRTEM, SAED and the elemental mapping scan for the sake of convenience.

Fig. 5 shows the TEM image of a large sized particle and the selected area is chosen for the HRTEM image. The sample show good crystallinity in a high resolution image. The lattice distance between two crystallographic planes was around 0.31 nm, which was matching with the ' d ' value of the (221) plane of $\text{Nd}_2\text{Fe}_{14}\text{B}$. The selective area electron diffraction (SAED) pattern of the same particle represents the crystalline pattern of the $\text{Nd}_2\text{Fe}_{14}\text{B}$ nanostructures. The diffraction pattern observed in the SAED image shows a good match with the X-ray diffraction peaks of $\text{Nd}_2\text{Fe}_{14}\text{B}$ for the (433), (431) and (650) plans. The peaks indicated in the HRTEM image and SAED pattern were confirmed from the values of the lattice distance of the respective planes.

The control of particle size can be achieved by carefully controlling various factors, such as the amount of precursor, fuel (glycine) and the nucleation rate during the initial step of water evaporation. The length of the complexing unit changes

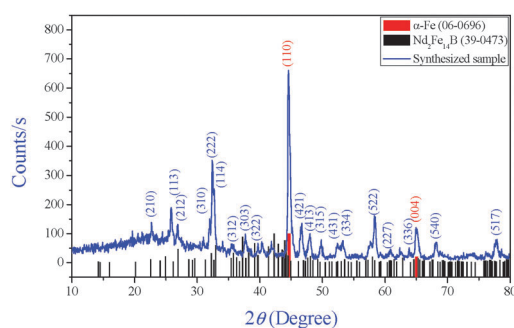


Fig. 3 XRD pattern of $\text{Nd}_2\text{Fe}_{14}\text{B}/\alpha\text{-Fe}$ nanostructures after reduction treatment at 950°C for 2 h in an $\text{Ar} + 5\% \text{H}_2$ gas atmosphere under vacuum.

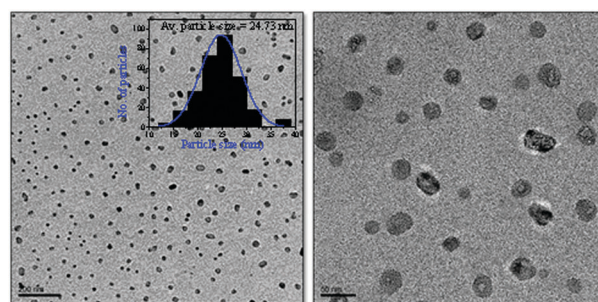


Fig. 4 TEM image of $\text{Nd}_2\text{Fe}_{14}\text{B}$ nanostructures after reduction at 950°C for 2 h in an $\text{Ar} + 5\% \text{H}_2$ gas atmosphere. The particle size histogram is shown in the inset. (scale – 200 nm.)

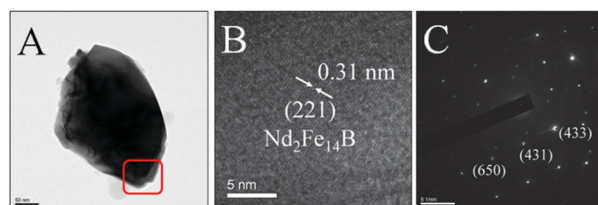


Fig. 5 TEM image representing (A) agglomerated area of $\text{Nd}_2\text{Fe}_{14}\text{B}$, (B) HRTEM of the selected area and (C) SAED pattern of the same area. The sample was reduced at 950°C for 2 h in an $\text{Ar} + 5\% \text{H}_2$ atmosphere. (Scale – 50 nm.)

with the amount of glycine added. This can also help to control the nucleation rate of the nanoparticles. During evaporation of the water, the metal cations, which are in the form of a complex with glycine molecules, starts nucleation and subsequent growth. The nanostructures of $\text{Nd}_2\text{Fe}_{14}\text{B}$ prepared by the wet chemistry route were earlier reported by Cha *et al.*,²⁶ Kang and Lee,²⁷ and Lee *et al.*²⁸ The precise control of the magnetic nanoparticles is highly responsible for its magnetic properties as the magnetic properties are highly dependent on the particle size.²⁹ In our case, the average particle size of $\text{Nd}_2\text{Fe}_{14}\text{B}$ is precisely controlled up to the 25 nm range.

During the high temperature reduction treatment of the metals, such as iron, neodymium and boron, they become uniformly diffused into each other. This interdiffusion is necessary for the perfect crystal structure of NdFeB alloy. To understand this metallic interdiffusion, elemental mapping scanning and EDX analysis of the large sized particles were carried out for $\text{Nd}_2\text{Fe}_{14}\text{B}$ and is shown in Fig. 6. We can clearly observe the homogeneous inter-diffusion of iron and neodymium into each other. Boron was excluded from the measurement since it is a light element and cannot be detected by this technique.³⁰ The obtained values of Nd and Fe from EDX analysis cannot be considered as exact values as the amount of boron present in the alloy is still unknown.

Fig. 7 shows TEM image of nanoparticles of $\text{Nd}_2\text{Fe}_{14}\text{B}/\alpha\text{-Fe}$ reduced at 950°C for 2 h in $\text{Ar} + 5\% \text{H}_2$ atmosphere. In this case we have obtained two different sized particles like previous case of $\text{Nd}_2\text{Fe}_{14}\text{B}$. The particle size estimated from Debye–Scherrer calculated at diffraction peaks of (222) and [(006) and (110)] was 17.45 and 26.58 nm, respectively. Since the peak of $\text{Nd}_2\text{Fe}_{14}\text{B}$ at $2\theta = 44.6^\circ$ overlaps with the peak of

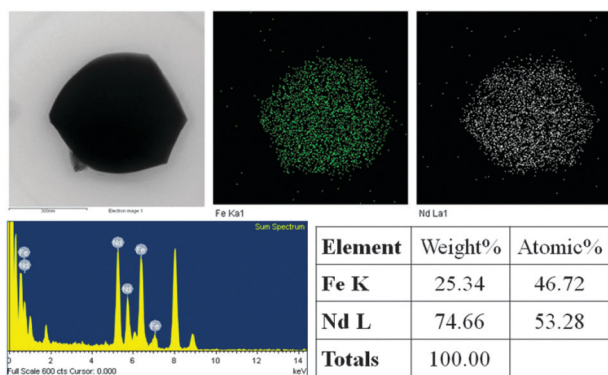


Fig. 6 Elemental mapping and EDX analysis of the large sized $\text{Nd}_2\text{Fe}_{14}\text{B}$ for understanding the inter-metallic diffusion of neodymium and iron into each other after the reduction treatment. Boron was excluded from the measurement. (Scale – 300 nm.)

α -Fe, it is difficult to mention whether the calculated particle size is of $\text{Nd}_2\text{Fe}_{14}\text{B}$ or α -Fe. The tiny particles having size around 10–12 nm and the larger agglomerated particles were chosen for HRTEM and EDX analysis.

To understand the crystallinity of the as-synthesized material, HRTEM image of large size nanoparticle (shown in Fig. 7) was obtained and shown in Fig. 8. The HRTEM image shows the good crystalline nature of the as-synthesized $\text{Nd}_2\text{Fe}_{14}\text{B}/\alpha$ -Fe nanostructures. The respective HRTEM of highlighted areas 'a', 'b' and 'c' are shown separately. The lattice parameters of 'a' and 'b' were matching with (301) and (204) plane of $\text{Nd}_2\text{Fe}_{14}\text{B}$ while area 'c' shows (110) plane of α -Fe phase. This gives us confirmation about the possible exchange coupling between $\text{Nd}_2\text{Fe}_{14}\text{B}$ and α -Fe.

The elemental mapping and EDX analysis of the $\text{Nd}_2\text{Fe}_{14}\text{B}$ and α -Fe phases are shown separately in Fig. 9 and 10, respectively. For elemental mapping, separate large sized agglomerated nanoparticles were selected to indicate the different phases formed, such as $\text{Nd}_2\text{Fe}_{14}\text{B}$ and α -Fe. The EDX data shows that the proportion of Nd and Fe in $\text{Nd}_2\text{Fe}_{14}\text{B}$ is close to each other. As the amount of boron is unknown we cannot consider this as the final composition of the alloy.

Fig. 10 shows that the interdiffusion of Fe and Nd into each other during heat treatment resulted in the homogeneous phase of the α -Fe nanostructure. The selected particle shows a high proportion of iron as compared to neodymium. The EDX data measured to estimate the proportion of Nd and Fe is also represented in Fig. 10. The atomic proportion of Fe is

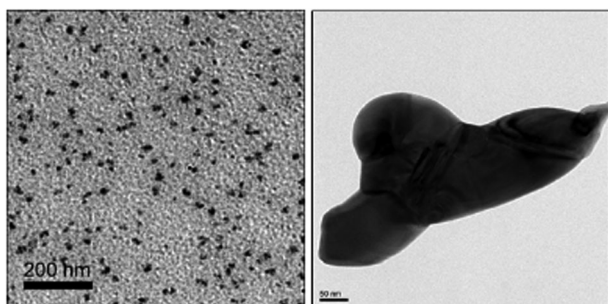


Fig. 7 TEM image of $\text{Nd}_2\text{Fe}_{14}\text{B}/\alpha$ -Fe nanostructures after reduction at 950 °C for 2 h in an Ar + 5% H_2 atmosphere. (Scale – 200 and 50 nm.)

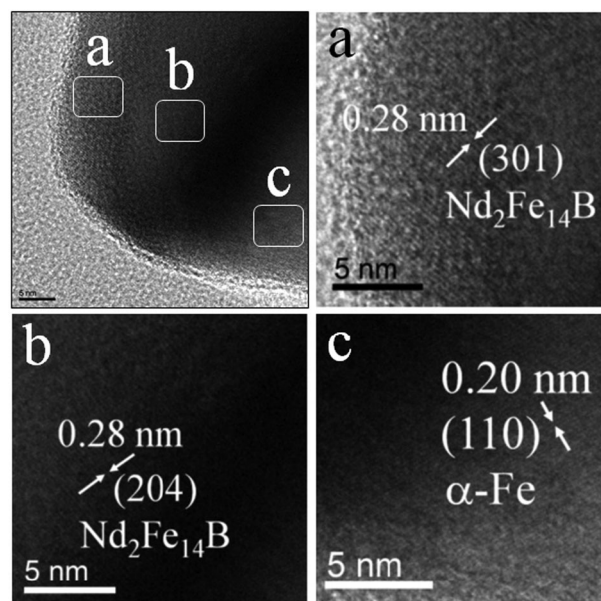


Fig. 8 HRTEM image of agglomerated nanostructures of $\text{Nd}_2\text{Fe}_{14}\text{B}/\alpha$ -Fe and HRTEM of the respective highlighted areas.

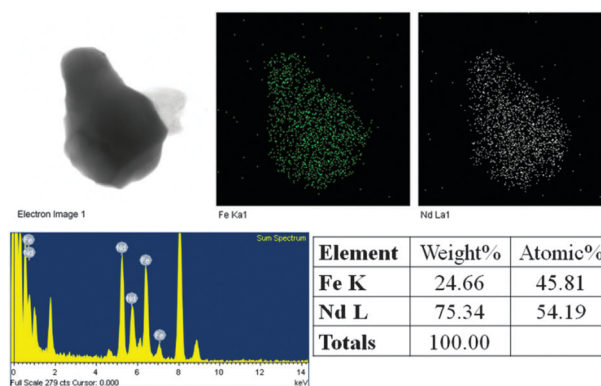


Fig. 9 Elemental mapping and EDX analysis of $\text{Nd}_2\text{Fe}_{14}\text{B}$ for understanding the interdiffusion of neodymium and iron into each other. Boron was excluded from the measurement. (Scale 300 nm.)

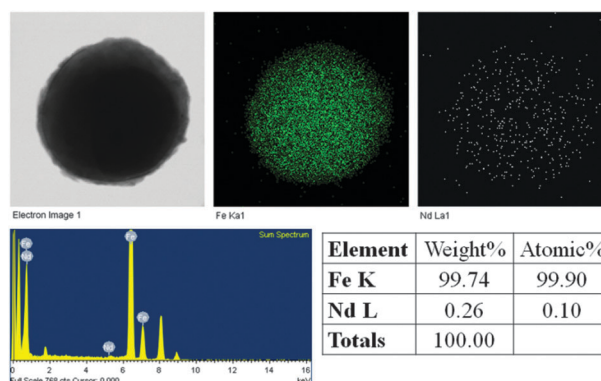


Fig. 10 Elemental mapping and EDX analysis of $\text{Nd}_2\text{Fe}_{14}\text{B}/\alpha$ -Fe for understanding the difference between the two phases. Boron was excluded from the EDX measurement. (Scale 300 nm.)

up to 99.9% while neodymium is present in only 0.1%, which indicates that this selected particle is of α -Fe.

The room temperature magnetization curves of the powder samples of $\text{Nd}_2\text{Fe}_{14}\text{B}$ and $\text{Nd}_2\text{Fe}_{14}\text{B}/\alpha\text{-Fe}$ were recorded at 14000 Gauss and are shown in Fig. 11. Curve (A) shows the magnetization curve of $\text{Nd}_2\text{Fe}_{14}\text{B}$ and curve (B) shows the magnetization curve of $\text{Nd}_2\text{Fe}_{14}\text{B}/\alpha\text{-Fe}$. In nanocomposites having hard and soft magnetic phases, theoretically, the maximum coercivity can be achieved only when the size of the soft phase is less than twice the domain wall thickness of the hard phase.³¹ Thus, for $\text{Nd}_2\text{Fe}_{14}\text{B}/\alpha\text{-Fe}$, the size of the soft phase should be close to or less than 10 nm. In our case as it was mentioned earlier, the proportion of large sized nanoparticles of both $\text{Nd}_2\text{Fe}_{14}\text{B}$ and $\text{Nd}_2\text{Fe}_{14}\text{B}/\alpha\text{-Fe}$ was much less in amount as compared to the small sized nanoparticles, so it is difficult to differentiate whether the obtained result is from the small sized nanoparticles or a larger one. Also since the particle size of the hard phase is not very different from the soft phase, it greatly affects the exchange coupling between the two phases. For the improvement of the energy product due to exchange coupling, the phases should be homogeneous with an appropriate volume fraction of the two phases.³² From the obtained plots, curve (A) shows the coercivity of 500.1326 G with a remanence (M_R) value of $3.7627 \text{ emu g}^{-1}$ and a saturation magnetization (M_S) of $10.901 \text{ emu g}^{-1}$. On the other hand, curve (B) of $\text{Nd}_2\text{Fe}_{14}\text{B}/\alpha\text{-Fe}$ shows the coercivity value of 268.7649 G with a remanence (M_R) value of $18.7290 \text{ emu g}^{-1}$ and a saturation magnetization (M_S) of $13947.0000 \text{ emu g}^{-1}$. In the case of the magnets, the extrinsic properties, such as remanent magnetization (M_R) and coercivity are dependent on the size and shape of the magnetic nanoparticles. In our case, we found that the hard phase magnetic nanoparticles were also in the size range of 20 nm or less. This is a very important point for the low magnetic property of the nanocomposite material.

Along with the size and shape of the nanoparticles, there are some factors which can directly affect the magnetic property, such as the chemical composition/phase purity, magnetic anisotropy and crystallinity. Magnetic properties are very sensitive to impurities which tend to occupy interstitial spaces in the lattice and impede the easy formation of the magnetic domains. Different phases formed during the reduction-diffusion process may lead to variation in the magnetic

property and thus the net magnetic property will be lower than expected.³³ Magnetic anisotropy is the main source of hysteresis and coercivity. Various types of anisotropies are directly associated with magnetic property of a material, such as magnetocrystalline anisotropy, shape anisotropy and exchange anisotropy. Lower magnetic anisotropy, in our case, has led to a lower coercivity value and lower magnetic property. In our case though, we could not find the presence of a different intermetallic phase other than $\text{Nd}_2\text{Fe}_{14}\text{B}$ and $\alpha\text{-Fe}$, the crystalline nature of the synthesized material might be responsible for the lower magnetic property. It is well known fact, that if the material is not perfectly crystalline then the domain wall thickness will not be sufficient to cause exchange coupling with the neighboring domain. The coercivity of the hard phase magnet arises from the large magnetocrystalline anisotropy of the material with a non-cubic structure.³⁴ The reason for obtaining the lower magnetic properties is by having a very small particle size of $\text{Nd}_2\text{Fe}_{14}\text{B}$ and $\text{Nd}_2\text{Fe}_{14}\text{B}/\alpha\text{-Fe}$ nanostructures. At hard phase magnetic particles, with diameters less than 50–60 nm in case of $\text{Nd}_2\text{Fe}_{14}\text{B}$ and $\text{Nd}_2\text{Fe}_{14}\text{B}/\alpha\text{-Fe}$, the material behaves like a super paramagnetic material because of Néels and Brownian motion. Further studies on the phase purity and increase of magnetic properties of the hard phase $\text{Nd}_2\text{Fe}_{14}\text{B}$ and nanocomposite material $\text{Nd}_2\text{Fe}_{14}\text{B}/\alpha\text{-Fe}$ are underway. The smooth hysteresis loop of $\text{Nd}_2\text{Fe}_{14}\text{B}/\alpha\text{-Fe}$ nanocomposite material indicates that the magnetic spin exchange between the hard phase $\text{Nd}_2\text{Fe}_{14}\text{B}$ and soft phase $\alpha\text{-Fe}$ are obviously exist in the composite material.

4. Conclusion

Synthesis of $\text{Nd}_2\text{Fe}_{14}\text{B}$ and $\text{Nd}_2\text{Fe}_{14}\text{B}/\alpha\text{-Fe}$ magnetic nanoparticles and nanocomposites was carried out in a one pot reaction *via* a glycine autocombustion reduction diffusion reaction. The particle size of the nanostructured material was carefully controlled by tuning the reaction parameters, such as metallic ratio, synthesis temperature and controlled reduction treatment. Excellent inter-diffusion of iron and neodymium was observed in both cases after the reduction treatment. The obtained magnetic properties of the nanostructured material is directly related to the average particle size, phase purity, crystallinity and exchange coupling between the hard and soft phase magnetic material.

Acknowledgements

The authors appreciate the financial support from the Joint Research Project of ISTK (Korea Research Council for Industrial Science and Technology).

Notes and references

- 1 M. Sagawa, S. Fujimura, N. Togawa, H. Yamamoto and Y. Matsuura, *J. Appl. Phys.*, 1984, **55**, 2083.
- 2 M. Sagawa, S. Hirosawa, H. Yamamoto, S. Fujimura and Y. Matsuura, *Jpn. J. Appl. Phys.*, 1987, **26**, 785.
- 3 J. F. Herbst, *Rev. Mod. Phys.*, 1991, **63**, 819.
- 4 J. F. Herbst and J. J. Croat, *J. Magn. Magn. Mater.*, 1991, **100**, 57.
- 5 Y. Kanko, *IEEE Trans. Magn.*, 2000, **36**, 3275.
- 6 Y. Hou and S. Sun, *Appl. Phys. Lett.*, 2007, **91**, 153117.
- 7 P. K. Deheri, V. Swaminathan, S. D. Bhame, Z. Liu and R. V. Ramanujan, *Chem. Mater.*, 2010, **22**, 6509.

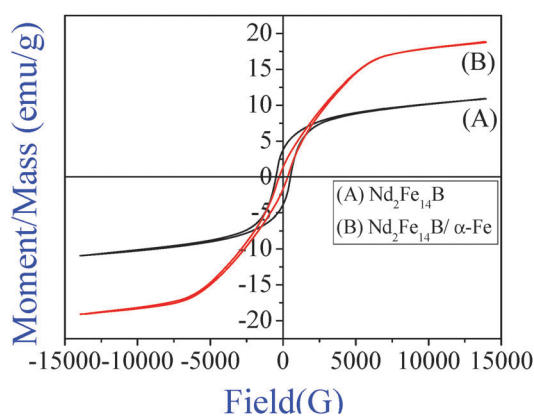


Fig. 11 Room temperature VSM measurement of (A) $\text{Nd}_2\text{Fe}_{14}\text{B}$ and (B) $\text{Nd}_2\text{Fe}_{14}\text{B}/\alpha\text{-Fe}$ nanostructures. The maximum field of a 14000 Gauss electromagnet was applied for the measurement.

- 8 E. F. Kneller and R. Hawig, *IEEE Trans. Magn.*, 1991, **27**, 3588.
- 9 J. F. Herbst, J. J. Croat and W. B. Yelon, *J. Appl. Phys.*, 1985, **57**(1), 4086.
- 10 N. G. Akdogan, W. Li and G. C. Hadjipanayis, *J. Appl. Phys.*, 2011, **109**, 07A759.
- 11 J. J. Croat, J. F. Herbst, R. W. Lee and F. E. Pinkerton, *J. Appl. Phys.*, 1984, **55**, 2078.
- 12 J. M. D. Coey, *J. Magn. Magn. Mater.*, 2001, **226–230**, 2107.
- 13 C. Yamahata, C. Lotto, E. Al-Assaf and M. A. M. Gijs, *Microfluid. Nanofluid.*, 2004, **1**, 197.
- 14 K. Ono, Y. Kakefuda, R. Okuda, Y. Ishii, S. Kamimura, A. Kitamura and M. Oshima, *J. Appl. Phys.*, 2002, **91**, 8480.
- 15 Y. Hou, Z. Xu, S. Peng, C. Rong, J. P. Liu and S. Sun, *Adv. Mater.*, 2007, **19**, 3349–3352.
- 16 H. W. Gu, B. Xu, J. C. Rao, R. K. Zheng, X. X. Zhang, K. K. Fung and C. Y. C. Wong, *J. Appl. Phys.*, 2003, **93**, 7589.
- 17 X. Teng and H. Yang, *J. Nanosci. Nanotechnol.*, 2007, **7**, 356.
- 18 J. H. Hong, W. S. Kim, J. I. Lee and N. H. Hur, *Solid State Commun.*, 2007, **141**, 541.
- 19 S. D. Bhame, V. Swaminathan, P. K. Deheri and R. V. Ramanujan, *Adv. Sci. Lett.*, 2010, **3**, 174.
- 20 T. Hyeon, *Chem. Commun.*, 2003, 927.
- 21 C. B. Murray, S. Sun, W. Gaschler, H. Doyle, T. A. Betley and C. R. Kagan, *IBM J. Res. Dev.*, 2001, **45**, 47.
- 22 L. A. Chick, L. R. Pederson, G. D. Maupin, J. L. Bates, L. E. Thomas and G. J. Exarhos, *Mater. Lett.*, 1990, **10**, 6.
- 23 K. Suresh and K. C. Patil, *J. Solid State Chem.*, 1992, **99**, 12.
- 24 E. E. Sileo, R. Rotelo and S. E. Jacobo, *Phys. B: Condens. Matter Quanta*, 2002, **320**, 257.
- 25 J. Huang, H. Zhuang and W. Li, *J. Magn. Magn. Mater.*, 2003, **256**, 390.
- 26 H. G. Cha, Y. H. Kim, C. W. Kim and Y. S. Kang, *IEEE Trans. Magn.*, 2006, **1**, 656.
- 27 Y. S. Kang and D. K. Lee, *Int. J. Nanosci.*, 2006, **5**(2 & 3), 315.
- 28 D. K. Lee, H. G. Cha, Y. H. Kim, C. W. Kim, E. S. Ji and Y. S. Kang, *J. Nanosci. Nanotechnol.*, 2009, **9**, 4453.
- 29 C. B. Rong, D. Li, V. Nandwana, N. Poudyal, Y. Ding, Z. L. Wang, H. Zeng and J. P. Liu, *Adv. Mater.*, 2006, **18**, 2984–2988.
- 30 J. Berlin, *Imaging & Microscopy magazine*, 2011, **13**, 19–21.
- 31 R. Fischer, T. Leineweber and H. Kronmüller, *Phys. Rev. B: Condens. Matter Mater. Phys.*, 1998, **57**, 10723.
- 32 H. Kronmüller and T. Schrefl, *J. Magn. Magn. Mater.*, 1994, **129**, 66.
- 33 P. K. Deheri, S. Shukla and R. V. Ramanujan, *J. Solid State Chem.*, 2012, **186**, 224–230.
- 34 H. Zijlstra, in *Permanent magnets; Theory in Ferromagnetic materials*, ed. E. P. Wohlfarth, North Holland, 1982, vol. 3, pp. 37–105.